PDF files are openly distributed for the educational purpose only.

Interior of Mars

Geophysical Constraints

> Mean Density, Moment of Inertia

Mean density known for some time

> GM = 42828.371901 km³ s⁻²,   GMM-2B Lemoine et al. (2001)
> G = 6.67259 × 10⁻²⁰ km³ s⁻² kg⁻¹, Cohen and Taylor (1999)
> M = 6.418552 × 10²³ kg

$$\bar{\rho} = \frac{M}{\frac{4}{3}\pi R^3} = 3.908965 \times 10^3 \text{ kg m}^{-3}, \quad 3.91242 \times 10^3 \text{ kg m}^{-3}, \quad 3.918647 \times 10^3 \text{ kg m}^{-3}$$

$$R = 3397 \text{ km} \qquad\qquad R = 3396 \text{ km} \qquad\qquad R = 3394.2 \text{ km}$$

Neumann et al. (2004) report an equivalent spherical volume radius of 3389.5 km, which gives $\bar{\rho} = 3935.0$ kg m⁻³ .

It was not until 1997 that we had a measurement of C (polar MOI) from the precession rate of Mars rotation axis due to the torque of the Sun on Mars' equatorial bulge. Prior to that, C had been inferred from the J_2 of Mars' gravitational field and arguments about hydrostatic equilibrium.

$$U = \frac{GM}{R}\left[1 + \sum_{l=2}^{\infty}\left(\frac{a_e}{r}\right)^l \sum_{m=0}^{l}\left\{ \overline{C}_{lm}\cos m\lambda + \overline{S}_{lm}\sin m\lambda \right\}\overline{P}_{lm}(\sin\phi) \right]$$

U = geopotential

a_e = reference equatorial radius

$\overline{P}_{lm}$ = normalized associated Legendre functions of degree l and order m. r, λ, ϕ are body-fixed spherical coordinates, radial distance, longitude, latitude

$\overline{C}_{lm}$, $\overline{S}_{lm}$ normalized coefficients

$$\overline{J}_2 = -\overline{C}_{20}$$
$$J_2 = \sqrt{5}\,\overline{J}_2 = -C_{20} = -\sqrt{5}\,\overline{C}_{20}$$

We will also use C_{22} and S_{22}

$$C_{22} = \sqrt{\frac{5}{12}}\,\overline{C}_{22} \qquad S_{22} = \sqrt{\frac{5}{12}}\,\overline{S}_{22}$$

From Mars Gravity Model MGS 951 (PDS website wwwpds.wustl.edu/missions/mgs/rsdata.html in volume MORS_1024)

$$\bar{J}_2 = 0.87502162 \times 10^{-3}$$

$$J_2 = 1.956607 \times 10^{-3}$$

$$\bar{C}_{22} = -0.84635663 \times 10^{-4}$$

$$C_{22} = -0.5463208 \times 10^{-4}$$

$$\bar{S}_{22} = 0.489345418 \times 10^{-4}$$

$$S_{22} = 0.3158711 \times 10^{-4}$$

$$\left(\bar{C}_{22}^2 + \bar{S}_{22}^2\right)^{1/2} = 9.776392 \times 10^{-5}$$

$$\left(C_{22}^2 + S_{22}^2\right)^{1/2} = 6.310634 \times 10^{-5}$$

For a planet in hydrostatic equilibrium

$$J_2 = \frac{1}{Ma^2}\left\{C - \frac{A+B}{2}\right\} \quad A,B,C \text{ are principal moments of inertia, a general formula}$$

$$= \frac{2}{3}f - \frac{1}{3}m \qquad \text{to first order in } m \text{ and } f$$

$$f = \text{flattening} \qquad m = \frac{a^3\omega^2}{GM}$$

$$f = \frac{5m/2}{1 + \left\{\frac{5}{2}\left(1 - \frac{3}{2}\frac{C}{Ma^2}\right)\right\}^2} \quad \text{Radau relation}$$

$\omega = 7.08821808 \times 10^{-5} \text{ rad s}^{-1}$ with $a = 3396$ km $\qquad m = 4.594577 \times 10^{-3}$

From J_2 and m we can solve for f and then C/Ma^2

$$\frac{C}{Ma^2} = \frac{2}{3} - \frac{4}{15}\left(\frac{5m}{2f} - 1\right)^{\frac{1}{2}}$$

$$\frac{C}{Ma^2} = \frac{2}{3} - \frac{4}{15}\left[\frac{\frac{5}{2}m}{\frac{3}{2}J_2 + \frac{m}{2}} - 1\right]^{\frac{1}{2}}$$

$$\frac{C}{Ma^2} = \frac{2}{3} - \frac{4}{15}\left[\frac{5m}{3J_2 + m} - 1\right]^{\frac{1}{2}}$$

What results for $\dfrac{C}{Ma^2}$ if we assume Mars is in hydrostatic equilibrium?

$$\frac{C}{Ma^2} = 0.375, \quad \text{Today we know this exceeds Mars'} \ \frac{C}{Ma^2}.$$

In the past, the major issue was the extent to which Mars is in hydrostatic equilibrium. How should the Mars J_2 be corrected to account for nonhydrostatic effects?

In 1979, Kaula proposed a simple and elegant way to get an answer to this question.

Consider $J_2 = J_2^{\text{HE}} + J_2^{\text{Tharsis}}$

$$J_2^{\text{Tharsis}} = \frac{1}{Ma^2}\left\{ C^{\text{Tharsis}} - \frac{A^{\text{Tharsis}} + B^{\text{Tharsis}}}{2} \right\}$$

Tharsis is along the A axis. Assume it is spherically symmetric about this axis.

$$A^{\text{Tharsis}} = 0, \quad C^{\text{Tharsis}} = B^{\text{Tharsis}}$$

$$J_2^{\text{Tharsis}} = \frac{1}{Ma^2}\left\{ \frac{B^{\text{Tharsis}} - A^{\text{Tharsis}}}{2} \right\} = \frac{1}{Ma^2}\frac{1}{2}\left\{ B - A \right\}, \text{if } B - A \text{ for Mars is due to Tharsis}$$

but
$$J_{22} = \left(C_{22}^2 + S_{22}^2 \right)^{1/2} = \frac{B - A}{4Ma^2}$$

$$J_2^{\text{Tharsis}} = 2 J_{22}^{\text{Mars}} \quad ! \quad = 2 \times 6.310634 \times 10^{-5}$$

$$= 1.262126 \times 10^{-4}$$

$$J_2^{\text{HE}} = 1.830394 \times 10^{-3}$$

Use this value to estimate $\dfrac{C}{Ma^2} = 0.365$!   Extremely close to measured value.

$\dfrac{J_2^{\text{Tharsis}}}{J_2^{\text{Mars}}} = 6.45 \times 10^{-2}$, In this sense Mars is close to hydrostatic equilibrium but a small departure makes a big difference in computing C/MR^2, which in turn makes a big difference for interior models of Mars.

What value of moment of inertia should be used in constraining spherically symmetric models of Mars' interior? The planet has 3 values, A, B, and C. One should use

$$I = \frac{A + B + C}{3}$$

Most models in the literature use C. It makes a difference.

In 1997 Folkner et al. reported a measurement of Mars' rotational axis precession rate due to the torque exerted on Mars' equatorial bulge by the Sun. They reported ω_p = -7576 ± 35 milliarc sec per year.

$$\omega_p = \frac{3}{2} J_2 \cos\varepsilon \left(1 - e^2\right)^{-3/2} \frac{n^2}{\omega\left(C/MR^2\right)}$$

$\omega_p = $ precession frequency

$\varepsilon = $ Mars' obliquity (angle between equatorial and orbital plane) $= 25.189417\,^{\circ}$

$e = $ orbital eccentricity $= 0.09341$

$n = $ mean motion $= 191.408\,^{\circ}\,\mathrm{yr}^{-1}$

$\omega = $ rotation rate $= 350.891985\,\mathrm{deg/day}$

Solving for $\dfrac{C}{MR^2}$ gives 0.3662 ± 0.0017

Most recent interior models in the literature use this value. But they should use I instead!

Yoder et al. (2003) update ω_p and C

$$\omega_p = \left(7597 \pm 25\right)\times 10^{-3}\,\mathrm{arc\ sec\ yr}^{-1}$$

$$\frac{C}{MR^2} = 0.3650 \pm 0.0012$$

This is exactly the Kaula value from the deduced J_2^{HE} !

The corresponding value of I that should be used in modeling is obtained as follows:

$$J_2 = \frac{1}{Ma^2}\left(C - \frac{A+B}{2}\right) = -C_{20}$$

$$\frac{A+B}{2Ma^2} = \frac{C}{Ma^2} + C_{20}$$

$$\frac{B-A}{4Ma^2} = J_{22}$$

$$\frac{A}{Ma^2} = C_{20} + \frac{C}{Ma^2} - 2J_{22}$$

$$\frac{B}{Ma^2} = C_{20} + \frac{C}{Ma^2} + 2J_{22}$$

$$\frac{I}{Ma^2} = \frac{A+B+C}{3Ma^2} = \frac{2}{3}C_{20} + \frac{C}{Ma^2}$$

Using the above values of $\dfrac{C}{Ma^2}$ and C_{20} we get

$$\frac{I}{Ma^2} = 0.3637 \pm 0.0012$$

Correct for Tharsis. Use $\dfrac{A^{\mathrm{Tharsis}}}{Ma^2} = 0,\ \dfrac{B^{\mathrm{Tharsis}}}{Ma^2} = \dfrac{C^{\mathrm{Tharsis}}}{Ma^2} = 4J_{22}$

$$\frac{I^{\mathrm{Tharsis}}}{Ma^2} = \frac{8}{3}J_{22} = 1.682835 \times 10^{-4},\ \frac{I^{\mathrm{HE}}}{Ma^2} = 0.3635 \pm 0.0012$$

Tharsis contributes little to the mean moment of inertia of Mars. The range of moment of inertia values for interior modeling of Mars is 0.3623 to 0.3647.

Models of Mars constrained by $\bar{\rho}$ and I/Ma^2 leave no doubt that Mars has a metallic core. We will look at these models in more detail later.

Body	C/Ma^2	$\bar{\rho} = (kg/m^3)$
Earth	0.3307	5514.8
Mars	0.3650	3912
Io	0.3782	3527.5
Europa	0.346	2989
Ganymede	0.3115	1942
Callisto	0.3549	1834

What is the state of the core? Solid, liquid, partially solidified? Yoder et al. (2003) measured the effect on the MGS orbit of the solar-induced tidal deformation of Mars and concluded that at least the outer part of the core of Mars is liquid.

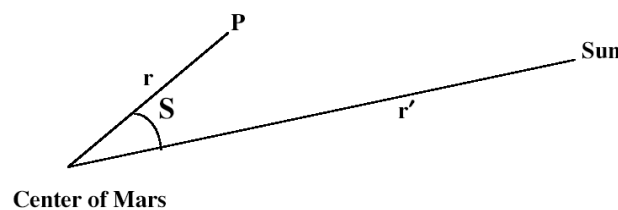The tide forcing potential on Mars due to the Sun is

$$\frac{GM_{Sun}}{r'} \sum_{\ell=2}^{\infty} \left(\frac{r}{r'}\right)^{\ell} P_{\ell}(\cos S)$$

where

r' is the distance from the center of Mars to the Sun

r is the distance from the center of Mars to P

S is the angle

The forcing potential distorts Mars and the resultant mass redistribution sets up a new potential described using Love numbers. For example, if we take just the $\ell = 2$ term, the forcing is

$$\frac{GM_{Sun}r^2}{r'^3} P_{20}(\cos S)$$

The potential from the tidally-induced deformation is written
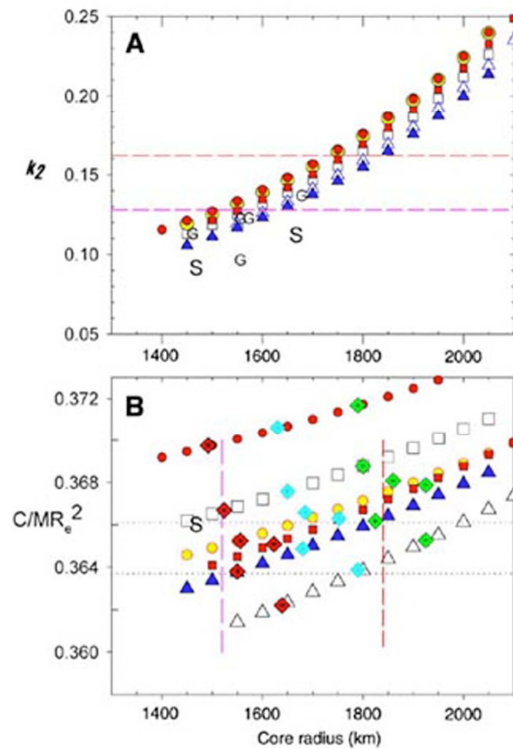
$$k_2 \frac{GM_{Sun}r^2}{r'^3} P_{20}(\cos S)$$

where k_2 is the Love number.

Yoder et al. (2003) find $k_2 = 0.153 \pm 0.017$.

To interpret this number, one must account for the contribution of atmospheric tides to k_2 and the effects of anelasticity in the mantle. Yoder et al. (2003) estimate that the elastic value of k_2 for Mars is 0.145 ± 0.017.

k_2 can be calculated for a model of Mars' interior by solving the equations of motion for the distorting potential.

Figure 2 of Yoder et al. (2003) shows that the acceptable range of k_2 implies a core radius for Mars between about 1500 km and 1850 km.

Figure 2 of Yoder et al. (2003). Model estimates of the elastic Love number k_2 (**A**) and moment of inertia C/MR_e^2 (**B**) versus core radius for a representative suite of structural models of Mars. These models vary χ_M [85% (triangles), 80% (boxes), and 75% (circles)] and ΔT [200 K (red and yellow), 0 K (white), and -200 K (blue)]. Crustal thickness is 50 km except for $\chi_M = 75\%$, $\Delta T = 200$ K, and $h_{cr} = 100$ km (yellow circles). Diamonds correspond to core $\chi_c = Fe/(Fe + FeS)$ of 25% (red), 50% (cyan), and 75% (green) in Fig. 2B. Constraints on C/MR_e^2 (dotted lines) from Eq. 7 and the inferred elastic $k_2 = 0.145 \pm 0.17$ (dashed lines) are also shown.

The k_2 of a model depends mainly on the product of mantle rigidity and thickness combined with the size and state of the core. The calculation in Yoder et al. (2003) assumes a liquid core.

A lower rigidity in the mantle, due, for example, to partial melting, could also contribute to the relatively large value of k_2.

Smith et al. (2001) claim $k_2 = 0.055 \pm 0.008$.

Van Hoolst et al. (2003) claim that the tidal signal is at the limit of detection and is too small to permit the inference of interior properties of Mars.

The Phobos tide is 8% of the solar tide.
The Deimos tide is 0.08% of the solar tide.

Van Hoolst et al. (2003) calculate Love numbers for a variety of Mars interior models.
Figure 9 of their paper shows results of the model calculations.
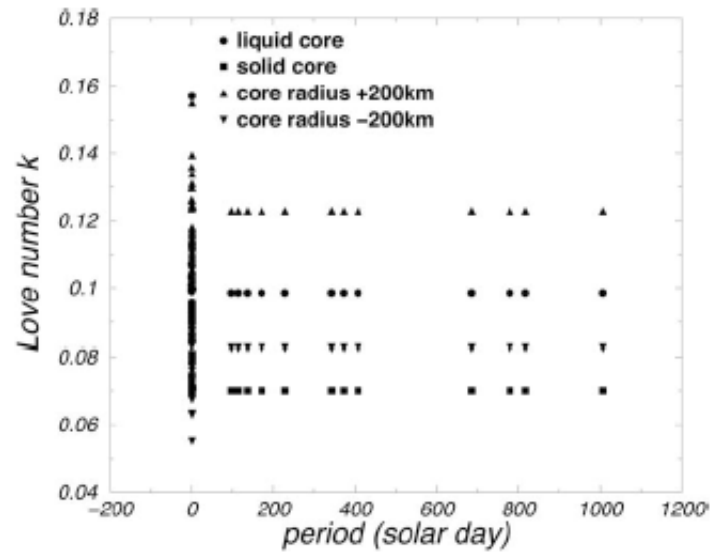
Figure 9 of Van Hoolst et al (2003). Second-degree Love number k for long-period tidal waves.

Love numbers are very sensitive to the core of Mars.
k_2 is about 0.1, about 3 times smaller than Earth's k_2. This is because Mars is smaller and its core is relatively smaller.

Interior Modelling

Simple 2 or 3 layer models of Mars can be constructed based on

$$\bar{\rho} = \rho_s + (\rho_c - \rho_m)\left(\frac{r_c}{R}\right)^3 + (\rho_m - \rho_s)\left(\frac{r_m}{R}\right)^3$$

$$\bar{\rho}\left(\frac{I}{MR^2}\right) = \frac{2}{5}\left[\rho_s + (\rho_c - \rho_m)\left(\frac{r_c}{R}\right)^5 + (\rho_m - \rho_s)\left(\frac{r_m}{R}\right)^5\right]$$

2 eqs., 5 unknowns r_c, r_m, ρ_s, ρ_m, ρ_c

Mantle and Core Densities and Core Mass Fraction
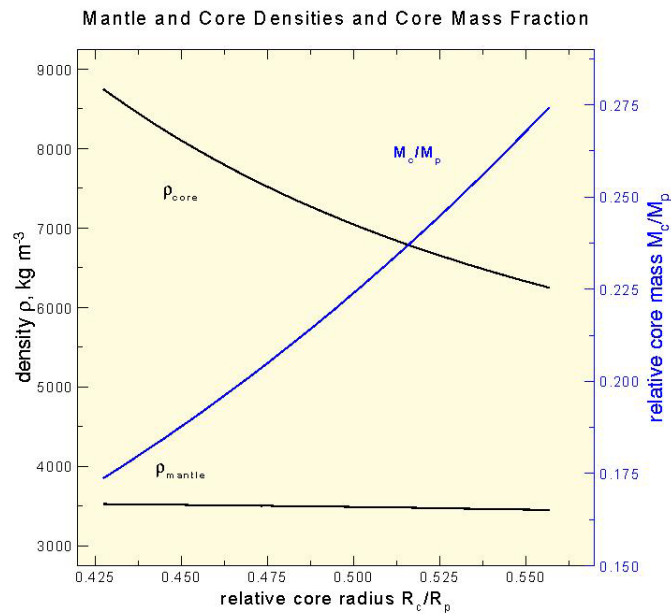
More complex models can be developed by integrating the following:

$$\frac{dm}{dr} = 4\pi r^2 \rho_r$$

$$\frac{dm_{Fe}}{dr} = x_{Fe}\frac{dm}{dr}$$

$$\frac{dI}{dr} = \frac{8}{3}\pi r^4 \rho_r$$

$$\frac{dg}{dr} = 4\pi G\rho - \frac{2g}{r}$$

$$\frac{dp}{dr} = -\rho_r g$$

6 unknowns p, ρ_r, g, I, m, m_{Fe} 5 eqs.   Need EOS $\rho = \rho(p)$

A simple EOS is

$$p = K_0 \left(\frac{\rho}{\rho_0} \right)^{K'}$$

where

$$K = \text{bulk modulus } = K_0 + K' p, \quad K = \frac{1}{\rho} \left(\frac{\partial \rho}{\partial p} \right)_T$$

If the EOS is temperature dependent, then T is another variable requiring an additional equation.

In terms of heat flux q

$$\frac{dq}{dr} = \rho_r \varepsilon_r - \frac{2q}{r}$$

ε_r = rate of heat production/mass.

In boundary layers

$$\frac{dT}{dr} = \frac{-q}{k}$$

k = thermal conductivity.
Otherwise the temperature is adiabatic

$$\frac{dT}{dr} = \left(\frac{dT}{dp} \right)_{ad} \frac{dp}{dr} = \frac{\gamma T}{K} \frac{dp}{dr}$$

γ = Grüneisen parameter = $\dfrac{\alpha K}{\rho c_p}$

α = thermal diffusivity
c_p = specific heat at constant pressure

Results from Sohl and Spohn (1997)

Sohl and Spohn (1997) investigate 2 end-member models, a geochemical-based one and a geophysical-based one

Geochemical-Based Model	Geophysical-Based Model
Assume bulk chondritic $\dfrac{\text{Fe}}{\text{Si}} = 1.71$	Assume $\dfrac{C}{MR^2} = 0.366$
$\downarrow$ leads to	$\downarrow$ leads to
$\dfrac{C}{MR^2} = 0.357$	$\dfrac{\text{Fe}}{\text{Si}} = 1.35$

Models suggest an Fe-Ni-FeS core a little less than $0.5R_p$, a silicate mantle with olivine $\rightarrow$ spinel phase change and a 100-250 km thick basaltic crust. No perovskite formation. Core sulfur content is 14 wt%. Core is entirely liquid.

It is impossible to satisfy the chondritic Fe/Si and C/MR^2 constraints simultaneously.

Assumptions –   The heat flow at the CMB is 3 mW m^{-2}. The SNC-derived composition from
Wänke and Dreibus (1988) is adopted. Crust is assumed to be basalt. Sulfur
in the core is assumed to be present as FeS with $\chi_S = 14.2\%$ by weight.
Birch-Murnaghan EOS.

MOI model, 'thin' crust 110 km thick, 'small' core 1468 km radius.

Fe/Si model, 'thick' crust 250 km thick, 'large' core 1667 km radius.

No sensitivity studies carried out.


Mars Interior Structure
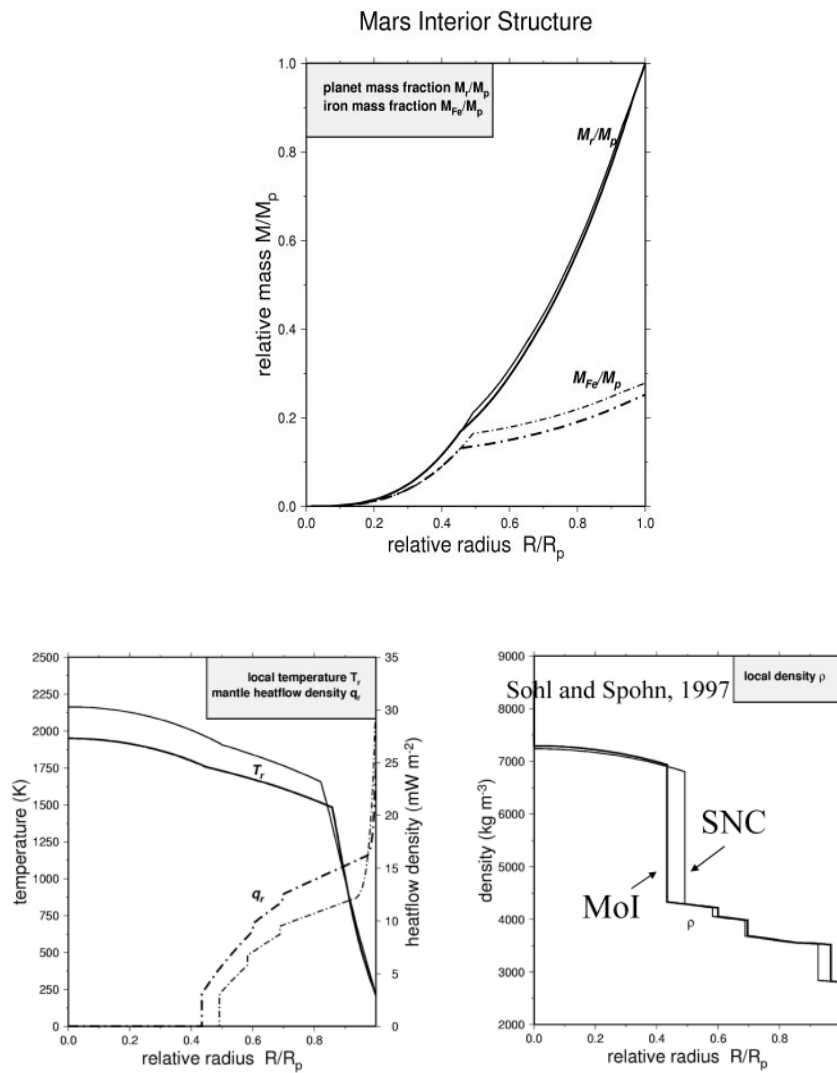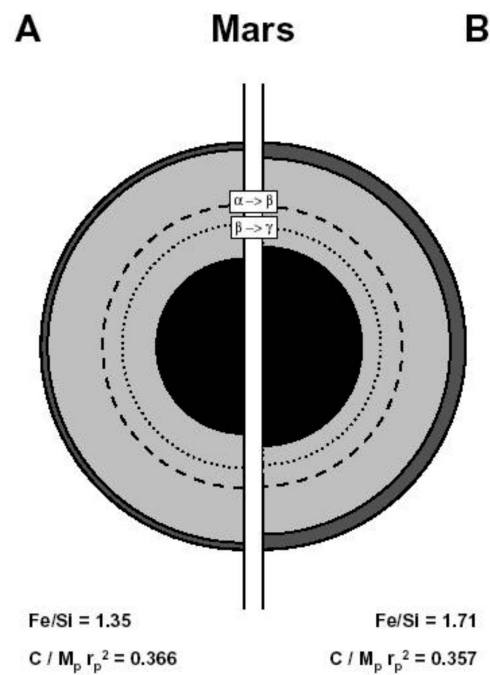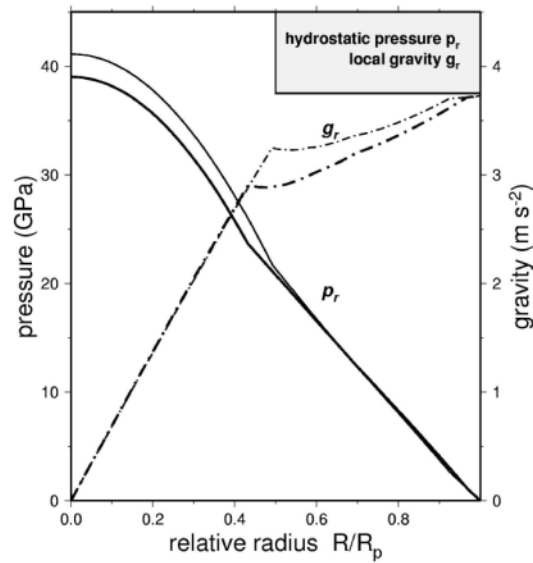
Figure 1 of Sohl and Spohn (1997). Comparison of the internal structure of Mars for both models A and B. The global structures of the two models are similar, with a basaltic crust, an upper and a lower mantle separated by the α-olivine to β-spinel transition, and a metallic core. The lower mantle is further subdivided into β-spinel and γ-spinel layers. The models differ significantly in the thicknesses of the crusts and the radii of the liquid cores. Fe/Si and $C/M_p r_p^2$ denote the calculated global iron to silicate ratio and the dimensionless polar moment of inertia factor, respectively.

Results from Folkner et al. (1997)

Consider models with mantle compositions χ_M = Mg/(Mg + Fe) between 89% (Earth) to 70% (highly Fe enriched).
Adopt 2 temperature profiles – earthlike + 200 K, earthlike −200 K.
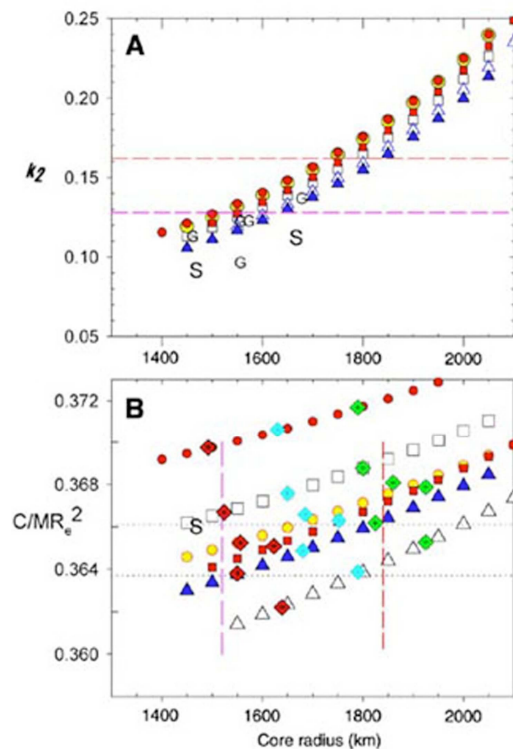Use $C/MR^2 = 0.3662 \pm 0.0017$.
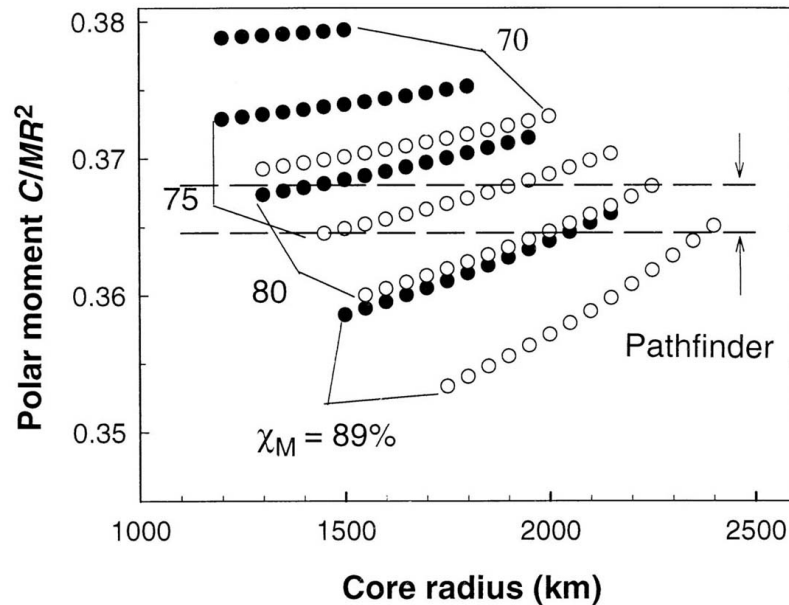
Figure 1 of Folkner et al. (1997). Polar moment of inertia versus core radius for four different mantle compositions and two different temperature profiles. The solid circles indicate models with temperatures 200 K lower than Earth at the same pressure; the open circles indicate models with temperatures 200 K higher than Earth.

Large range in core radius possible. Core radius can be further constrained by assumptions of core composition.

Results from Yoder et al. (2003)

Consider similar ranges of models as in Folkner et al. (1997).
Consider crustal thickness in the range of 50 to 100 km.

Figure 2 of Yoder et al. (2003). Model estimates of the elastic Love number k_2 (**A**) and moment of inertia C/MR_e^2 (**B**) versus core radius for a representative suite of structural models of Mars. These models vary χ_M [85% (triangles), 80% (boxes), and 75% (circles)] and ΔT [200 K (red and yellow), 0 K (white), and – 200 K (blue)]. Crustal thickness is 50 km except for $\chi_M = 75\%$, $\Delta T = 200$ K, and $h_{cr} = 100$ km (yellow circles). Diamonds correspond to core $\chi_c = Fe/(Fe + FeS)$ of 25% (red), 50% (cyan), and 75% (green) in Fig. 2B. Constraints on C/MR_e^2 (dotted lines) from Eq. 7 and the inferred elastic $k_2 = 0.145 \pm 0.17$ (dashed lines) are also shown.

k_2 estimate constrains r_c between 1520 km and 1849 km.
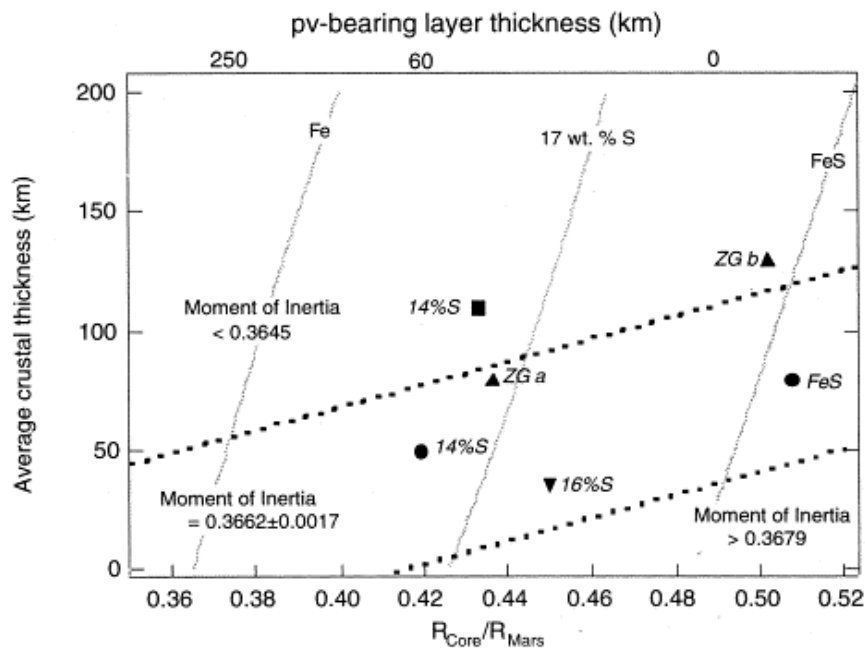Use $C/MR^2 = 0.3650 \pm 0.0012$.
A range of I/MR^2 of 0.3623 to 0.3647 defines a very different set of acceptable models!

<u>Results from Kavner et al. (2001)</u>

Use new measurements of density of FeS at high p,T to constrain Mars interior models.
Use a density profile for the mantle from Bertka and Fei (1998).
Vary crustal thickness and crustal density.

Figure 7 of Kavner et al. (2001). Interior structure models for Mars. Thick dotted lines constrain the range of acceptable models. Thin dotted lines show the range of solutions for a given core sulfur content. The figure illustrates the tradeoff between the allowable average crust thickness and the density and radius of the core. The thickness of the perovskite layer is indicated on the top axis. Previous estimates are also depicted as follows: open circles with sulfur contents labeled [30]; squares [2]; downward triangles [36]; upward triangles [35] (core sulfur content not calculated).

Consider C/MR^2 between 0.3645 and 0.3679. The I/MR^2 range of 0.3623 to 0.3647 implies a much thicker Martian crust. This changes the authors' conclusion. Perovskite layers are allowed by the models.

<u>Results from Gudkova and Zharkov (2004)</u>

Assume that hydrogen is incorporated into the core. Hydrogen in the core reduces its density and melting point.

Use a model of the crust that contains a porous layer and assume a basaltic composition based on SNC meteorites.
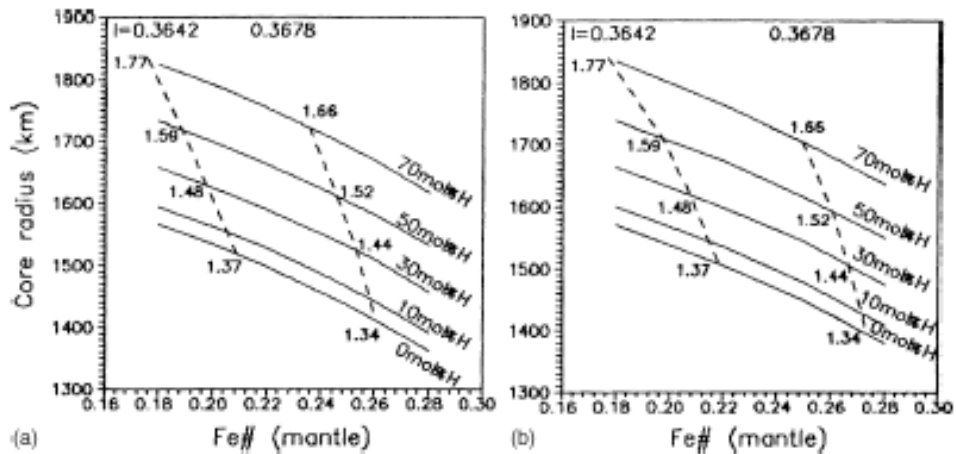
Use the Bertka and Fei (1997) mineral assemblages for the mantle.

Use Birch-Murnaghan EOS.

Change Fe content of mantle and modify mantle density profile accordingly.

Assume core is hydrogen, Fe and S with 14.2 wt.% S.

Assume I/MR^2 in the range 0.3642 to 0.3678.

Figure 9 of Gudkova and Zharkov (2004). Core radius as a function of Martian mantle Fe#, assuming a core composition of 14 wt.% S and a 50 km thick crust (a), and a 100 km thick crust (b) for different amount of hydrogen in the core (0-70 mol%). Dashed lines show the lower (left) and upper (right) limits of the moment of inertia factor. Fe/Si ratio is given for boundary models.

Hydrogen in the core leads to an increase in Fe/Si ratio and a decrease of Fe # in mantle due to an increase of r_c.

The chondritic Fe/Si ratio can be attained with hydrogen in the core.
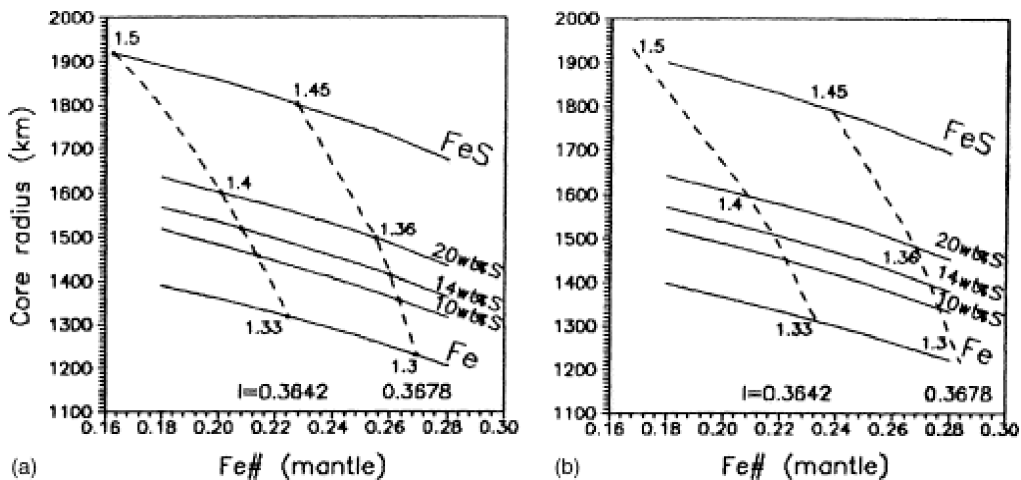
Figure 10 of Gudkova and Zharkov (2004). Core radius as a function of Martian mantle Fe# for a core composition ranging from 0 wt% S (FeS core) to 36 wt.% S (FeS core) assuming a 50 km thick crust (a) and a 100 km thick crust (b). Dashed lines show the lower (left) and upper (right) limits of the moment of inertia factor. Fe/Si ratio is given for boundary models.

Influence of core S content on core radius.
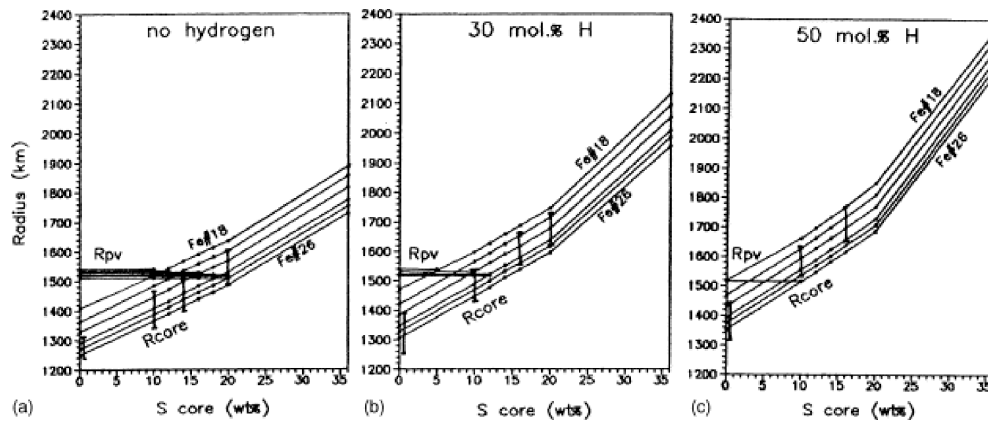
Figure 11 from Gudkova and Zharkov (2004). Core radius as a function of S wt.% in the core for different Martian mantle Fe# (18, 20, 22, 24, 25, 26) assuming a 50 km thick crust (a, no hydrogen in the core; b, 30 mol%; c, 50 mol% of hydrogen in the core). The horizontal lines mark the depth to the perovskite stability field, the beginning of the lower mantle. Vertical lines indicate the limits of the moment of inertia factor.

Perovskite layers can exist in the mantle for S sufficiently small (depending on H concentration in the core). The addition of H into the core increases r_c and decreases the thickness of the pv layer.

<u>Results from Bertka and Fei (1998)</u>

Assume $\qquad$ $C/MR^2 = 0.3662$
DW mantle density profile
Crust of density 3000 kg m^{-3}

Consider core compositions Fe, FeS, FeH, Fe$_7$C$_3$, Fe$_3$O$_4$
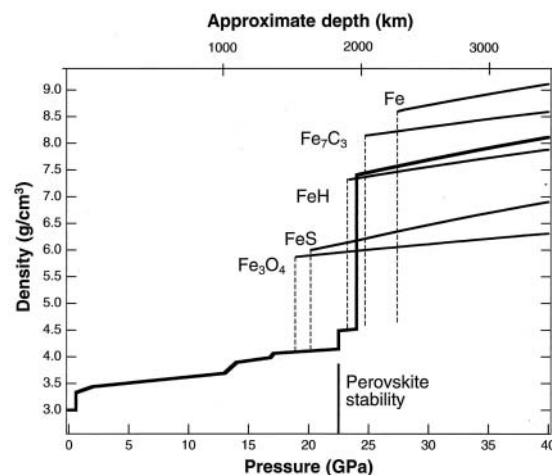
Figure 1 of Bertka and Fei (1998). Density profile of the DW model Martian mantle and core composition (Fe + 14 weight % S) (9) (thick solid line) and density profiles for a range of model core compositions (thin solid lines). Dashed lines indicate the depth, or pressure, of the core-mantle boundary for model core compositions. The mantle profile is shown with a 50-km, 3.0 g/cm^3 crust. The depth to the perovskite stability field (the beginning of the lower mantle) is also shown.

Conclude that the addition of H and C to a S-rich Fe core cannot increase the bulk Fe wt.% or Fe/Si ratio to C1 values while maintaining the constraint of a DW mantle and $C/MR^2 = 0.3662$.

Bulk Fe content of a C1 chondrite is 27.8 wt.% and Fe/Si ratio is 1.71.

Mars Crustal Thickness

Estimates of the thickness of the Martian crust come mainly from analysis of gravity and topography data.

But crustal thickness estimates have also come from:
    Studies of viscous relaxation of topography.
    Geochemical mass balance modeling (radiogenic elements, Nd isotopes).

Zuber et al. (2000) determined global crustal thickness variations using MGS topography and gravity data.

Figure 1 of Zuber et al. (2000) shows A (topography), B (free-air gravity), C (crustal thickness). Model assumes ρ_c = 2900 kg m^{-3}, ρ_{mantle} - ρ_{crust} = 600 kg m^{-3}, ρ_{Mars} = 3930 kg m^{-3}.
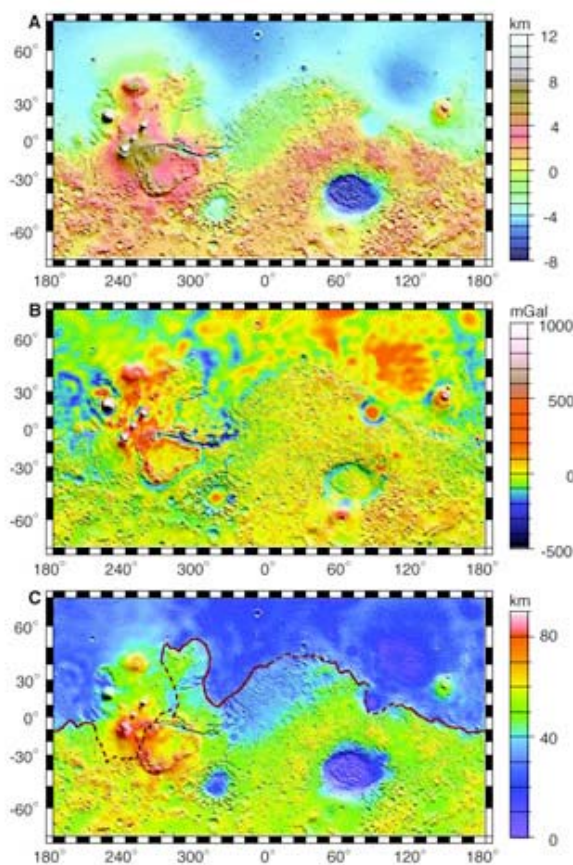
Figure 1 of Zuber et al. (2000). Global maps of (A) topography, (B) free-air gravity, and (C) crustal thickness (8) of Mars (Mercator projection). On all panels, the Tharsis province is centered near the equator in the longitude range 220° to 300°E and contains the east-west-trending Valles Marineris canyon system and the major volcanic shields Olympus Mons (0°, 247°E), and Arsia Mons (9°S, 239°E). The Arabia Terra region is centered at 10°N, 10°E, the Elysium rise is at 30°N, 159°E, the Tempe Terra region lies at 40°N, 290°E, the Syria Planum region is centered at 25°S, 270°E, and the Terra Cimmeria region is centered at 69°S, 180°E. Major impact basins include Hellas (45°S, 70°E), Argyre (50°S, 320°E), Isidis (12°N, 88°E), and Utopia (45°N, 110°E). The hemispheric dichotomy boundary is shown as a red line in (C), solid where distinctively expressed and dashed where estimated. This analysis uses an areocentric coordinate convention with east longitude positive. One degree of latitude on Mars equals ~59 km.

Zuber et al. (2000) report an average crustal thickness of 50 km, a minimum thickness of 3 km beneath the Isidis basin, a maximum thickness of 92 km in Syria Planum region.

Figure 2 of Zuber et al. (2000) shows how crust thins from southern hemisphere to northern hemisphere.
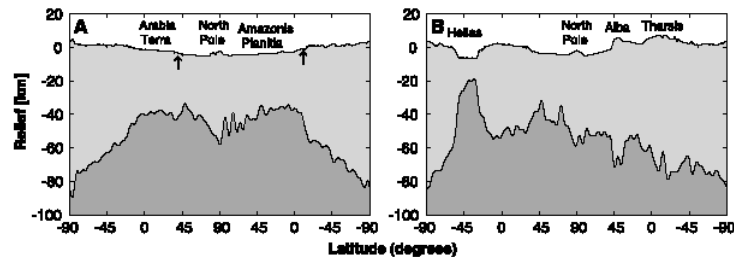
Figure 2 of Zuber et al. (2000). Circum-Mars profiles of crustal thickness along longitude lines of (A) 0° to 180^oE and (B) 70° to 250^oE. Light gray represents crust, and dark gray represents mantle. In the figures, the south pole is at both ends of the plot, the north pole is at the center, and the lower longitude profiles (0^oE and 70^oE) are on the left sides of the plots. Apparent crustal thickening beneath the north and south polar regions is an artifact of the assumption that layered terrains and ice caps are composed of material with the same density as the crust rather than less dense ice plus dust. The arrows in (A) show the location of the hemispheric dichotomy boundary. The vertical exaggeration is 30:1.

The thinning of the crust towards the north pole is also indicated in Figure 3 of Zuber et al. (2000).
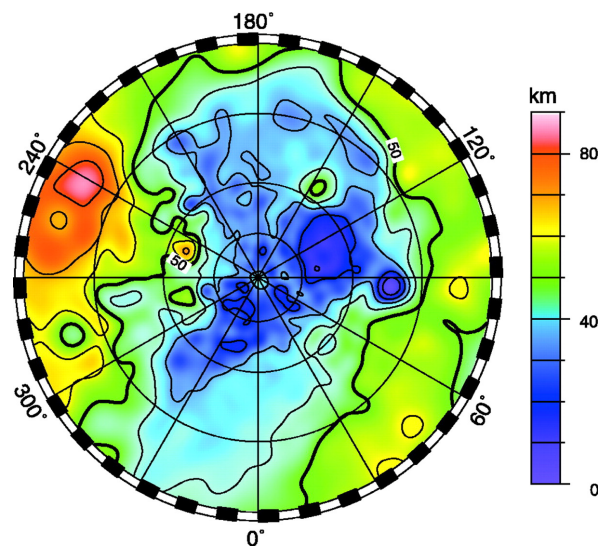
Figure 3 of Zuber et al. (2000). Polar stereographic projection of Martian crustal thickness. The figure encompasses latitudes from 20^oS to 90^oN. The contours are at intervals of 5 km.

The inferred 50 km mean crustal thickness is a consequence of the a priori assumption that the minimum crustal thickness beneath Isidis is 3 km (and assuming ρ_c = 2900 kg m^{-3} and ρ_m = 3500 kg m^{-3}).

Wieczorek and Zuber (2004) point out that this mean crustal thickness was mistakenly "referenced" to mean equatorial radius and not mean planetary radius. They correct this mean thickness downward to 44 km. They also redo the analysis for ρ_c = 2700-3100 kg m^{-3} and ρ_m = 3400-3550 kg m^{-3} and find that the mean crustal thickness is > 32 km.

The process for inferring crustal thickness uses the spherical harmonic representations of free-air gravity and topography to calculate the Bouguer anomaly (correction for topography). This requires an assumption of ρ_c and the knowledge of the mean planetary radius.

The Bouguer anomaly is then downward continued to the crust-mantle interface and the topography on this interface is determined. This requires an assumption of ρ_m and an assumption about the mean radius of the C-M interface.

Wieczorek and Zuber (2004) use the concept of the geoid topography ratio to calculate the thickness of the crust over the southern highlands. To first order, the GTR is (Turcotte and Schubert, 1982)

$$GTR = \frac{\Delta N}{h} = \frac{2\pi G \rho_c}{g} H = \frac{2\pi \rho_c R^2}{M} H$$

ΔN = geoid height, h is the surface elevation.
H is the crustal thickness at zero elevation. This is valid for cartesian geometry in the long wavelength limit. This simple approach is more complicated in spherical geometry.

A representative GTR for Mars is 15 m km^{-1}.

Many regions are excluded from the analysis of Wieczorek and Zuber (2004). These include: the Tharsis plateau, Argyre and Isidis basins, south polar ice cap, northern lowlands, Syrtis Major and other volcanic constructs.

The load and flexure of Tharsis influences the gravity and topography of Mars essentially everywhere. This effect needs to be corrected. One way is to remove low order and degree terms from the spherical harmonics of gravity and topography.

Wieczorek and Zuber (2004) obtain a mean crustal thickness for the region studied of 57 ± 24 km.

Turcotte et al. (2002) studied the geoid-topography relation along a polar track through the Hellas basin. It is assumed that the Hellas basin is fully isostatically compensated by crustal thickness variations (Airy compensation). For a constant density crust, the aeroid anomaly ΔN is related to topography by (Turcotte and Schubert, 1982, eq. 5-148)

$$\Delta N = \frac{2\pi \rho_c G}{g} \left\{ hH + \frac{1}{2} \left(\frac{\rho_m}{\rho_m - \rho_c} \right) h^2 \right\}$$

H is the zero-elevation crustal thickness. Topography and geoid anomaly data are fit along the track at 60ºE longitude with a quadratic equation as above. It is assumed that $\rho_m = 3500$ kg m^{-3}. From the quadratic terms of the fit and the scatter in the data it is determined that

$$\rho_c = 2960 \pm 50 \text{ kg m}^{-3}.$$

$$H = 90 \pm 10 \text{ km}.$$

The thickness of the crust in the deepest part of the basin ($h = -9$ km) is 33 km.

Estimates of average Martian crustal thickness differ by a factor of 2!
Only seismology will settle the question.

An update of the Zuber et al. (2000) global crustal thickness model has recently been carried out by Neumann et al. (2004).

Neumann et al. (2004) assume a mean crustal thickness of 45 km.

The Bouguer gravity anomaly map is shown in Figure 3 of Neumann et al. (2004)
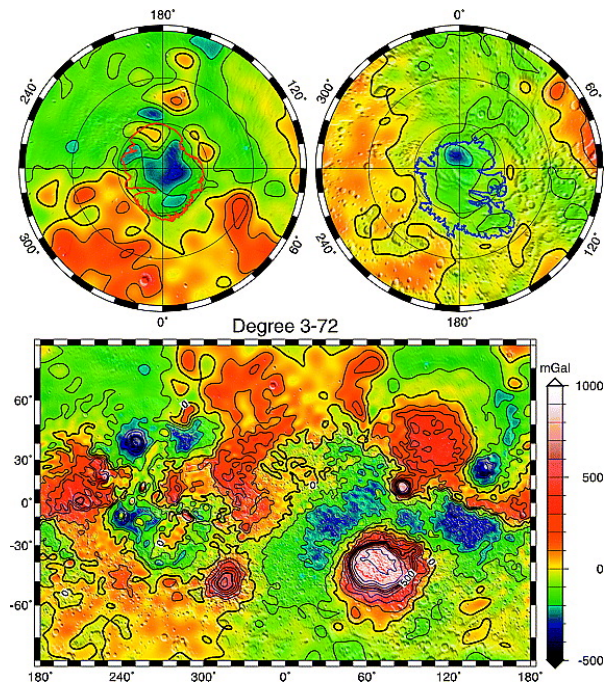
Figure 3 of Neumann et al. (2004). Color-contoured map of Bouguer anomaly, in Mercator (−75 to 75°) and polar stereographic (60-90°N, left; 60-90°S, right) projections, with shaded relief map for context. Contour interval is 100 mGal. Degree 1 and degree 2 terms are omitted. Outlines of the polar layered terrain are shown in polar projections.

The Isidis, Argyre, Utopia, and Hellas basins have large positive circular anomalies due to Moho uplift following impact.

Alba Patera, Tempe Terra, and the Elysium rise have highly negative anomalies due to compensation of mountains by thicker crust.

Bouguer anomalies are negative over both poles.

Figure 5 of Neumann et al. (2004) shows that the crust thickness has a bimodal character.

QuickTime™ and a
GIF decompressor
are needed to see this picture.

Figure 5 of Neumann et al. (2004). Histogram of crustal thickness, the difference between surface and mantle relief, versus area.

The two major peaks in Figure 5 are at 32 km and 58 km. The heavily cratered highlands contribute to the 58 km peak. The lowlands contribute to the 32 km peak. The narrow 58 km peak results from the relatively uniform thickness of the southern hemisphere crust. The northern lowlands crust shows a latitudinally varying crustal thickness and defines a broader peak at 32 km.

Crustal thickness variations along selected longitudinal transects are shown in Figure 6 of Neumann et al. (2004).

QuickTime™ and a
GIF decompressor
are needed to see this picture.

Figure 6 of Neumann et al. (2004). Crustal structure showing the pole-to-pole variations along three longitudinal great circle transects. Regions at the poles and through Arsia Mons that have been modeled with local density anomalies are shown in lighter shades. Vertical exaggeration 60:1.

Figure 6 shows that the thickest crust of Mars lies below the Arsia Mons volcanic construct in southern Tharsis.

The crustal thickness model of Neumann et al. (2004) is shown in Figure 7 from their paper.
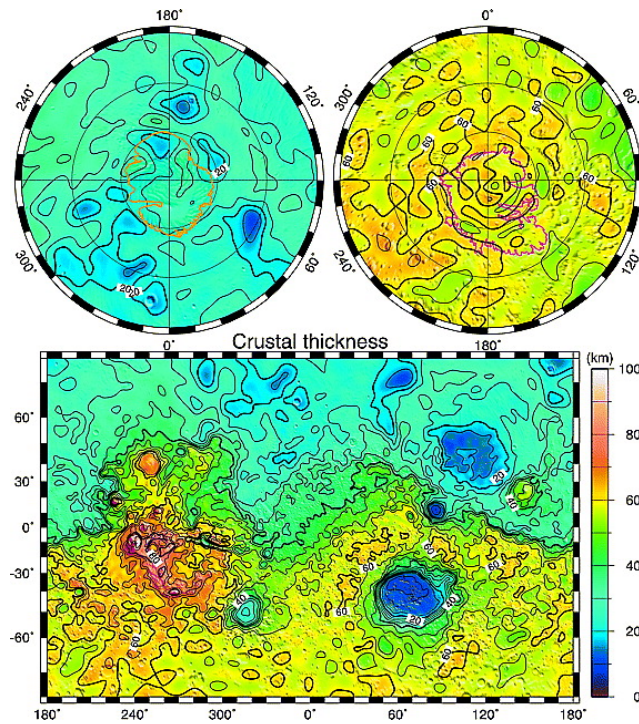
Figure 7 of Neumann et al. (2004). Degree 1-85 crustal thickness model (5 km contours), in Mercator and polar stereographic projections as in Figure 3.

## Mantle Phase Changes and Convection in Mars and Earth

We have seen that the olivine $\rightarrow$ spinel phase transformation occurs in the Martian mantle and that the spinel $\rightarrow$ perovskite phase change might occur near the base of the Martian mantle if the core is small enough.

These phase transitions could have important consequences for the dynamics of the Martian mantle.

Weinstein (1995), Harder and Christensen (1996), and Harder (1998) have shown that the spinel $\rightarrow$ perovskite phase change just above the CMB in Mars would tend to focus upwelling into a single plume. This offers a possible explanation for the dominance of Tharsis in the geology of Mars.

The spinel-pv phase change has this effect because it is endothermic and tends to retard the upward motion of plumes. A plume must become larger, i.e., accumulate more buoyancy, before it can penetrate the phase change.

Thermally induced phase boundary distortions occur in response to any mantle thermal anomaly such as the positive thermal anomaly associated with mantle plumes. The figure illustrates the distortion of the olivine-spinel and spinel-perovskite phase boundaries due to the upward motion of a hot mantle plume. The olivine-spinel phase boundary is displaced downward in the hot plume while the spinel-perovskite phase boundary is moved upward. The downward distortion of the olivine-spinel phase change makes the plume lighter than its surroundings thereby promoting plume upwelling. The upward distortion of the spinel-perovskite phase change makes the plume heavier than its surroundings and tends to retard plume upwelling.

(a) Exothermic (Olivine-Spinel)


(b) Endothermic (Spinel-Perovskite)
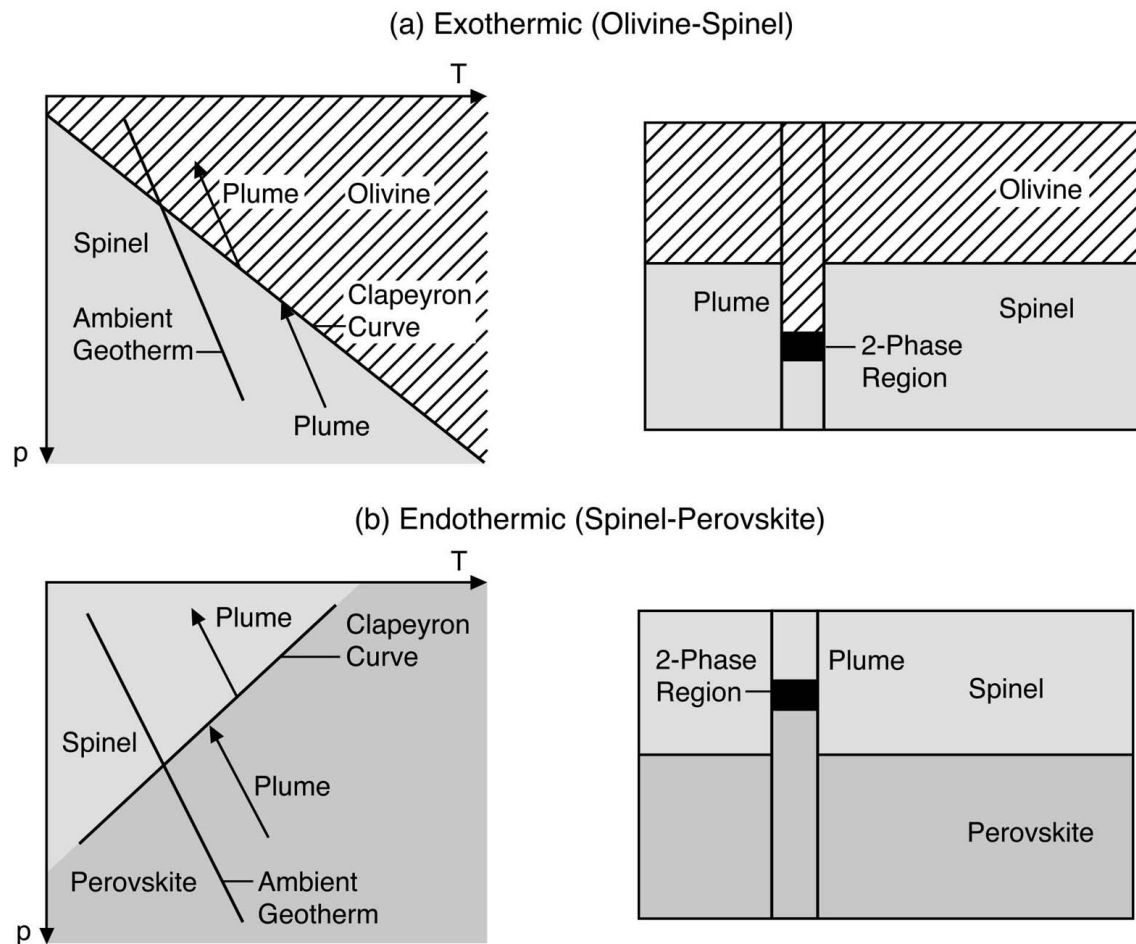
Figure 4.42 from Schubert et al. (2001). Sketch of equilibrium phase boundary displacement in a hot plume ascending through (a) the exothermic olivine-spinel phase change and (b) the endothermic spinel-perovskite phase change. Motion through the phase transitions results in narrow 2-phase regions in the plume. The positive Clapeyron slope of the exothermic phase change lowers the phase boundary in the plume while the negative Clapeyron slope of the endothermic phase change elevates the phase boundary in the plume. The *p-T* diagrams on the left show the path of the ascending plume and the Clapeyron curves separating the phases. Univariant phase transitions are assumed.

Latent heat release and absorption also influences mantle plumes moving upward through the transition zone. Latent heat is released when an upwelling plume moves through the spinel-perovskite phase change. The warming contributes to plume buoyancy through thermal expansion but it also tends to upwarp the phase boundary which tends to retard plume upwelling. Latent heat is absorbed when a plume rises through the olivine-spinel phase change which tends to cool the plume and retard its upflow. The cooling also tends to upwarp the phase boundary which adds to the negative buoyancy opposing plume upwelling. The phase change effects on mantle thermal anomalies and associated upflows and downflows are summarized in the Table.

Table 4.6 of Schubert et al. (2001). Summary of Dynamical Effects of Mantle Phase Changes			
Phase Change	**Phase Boundary Distortion by Advection of Thermal Anomalies**	**Phase Boundary Distortion Due to Release or Absorption of Latent Heat**	**Expansion or Contraction Due to Release or Absorption of Latent Heat**
Exothermic (olivine-spinel)	Enhances hot upwelling and cold downflow	Retards	Retards
Endothermic (spinel-perovskite)	Retards hot upwelling and cold downflow	Retards	Enhances

Recently, laboratory experiments and theoretical calculations (Murakami et al., 2004; Oganov and Ono, 2004, and Tsuchiya et al., 2004) have shown that perovskite transforms to a post-perovskite phase just above the CMB in the Earth.
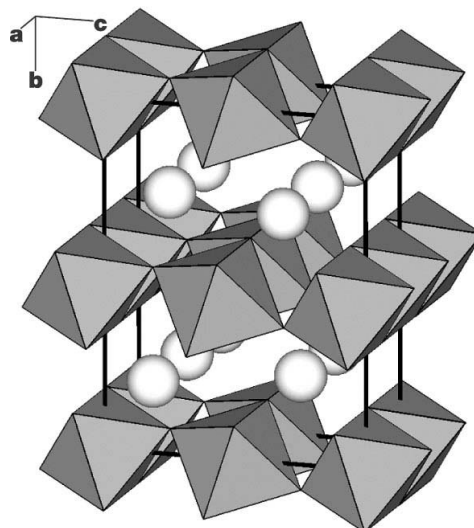

Figure 1 of Oganov and Ono (2004). Structure of the post-perovskite phase of $MgSiO_3$ (calculated at 120 GPa). SiO_6 octahedra and Mg atoms (spheres) are shown. Similar structures are known for Fe_2O_3, $CaIrO_3$, $FeUS_3$, $PbTlI_3$, $UScS_3$, $KTmI_3$, $AgTaS_3$ and $CaInBr_3$.

Earth and Mars are therefore similar in having solid state phase transitions at the base of their mantles (assuming the Martian phase transition exists). However, an important difference between Earth and Mars is that the phase change at the bottom of Earth's mantle is exothermic. The calculated Clapeyron slope of the pv $\rightarrow$ ppp is about 8 MPa K^{-1} and the phase change involves a density change of around 1.5%. Nakagawa and Tackley (2004) have investigated how an exothermic phase change at the base of Earth's mantle influences mantle convection.
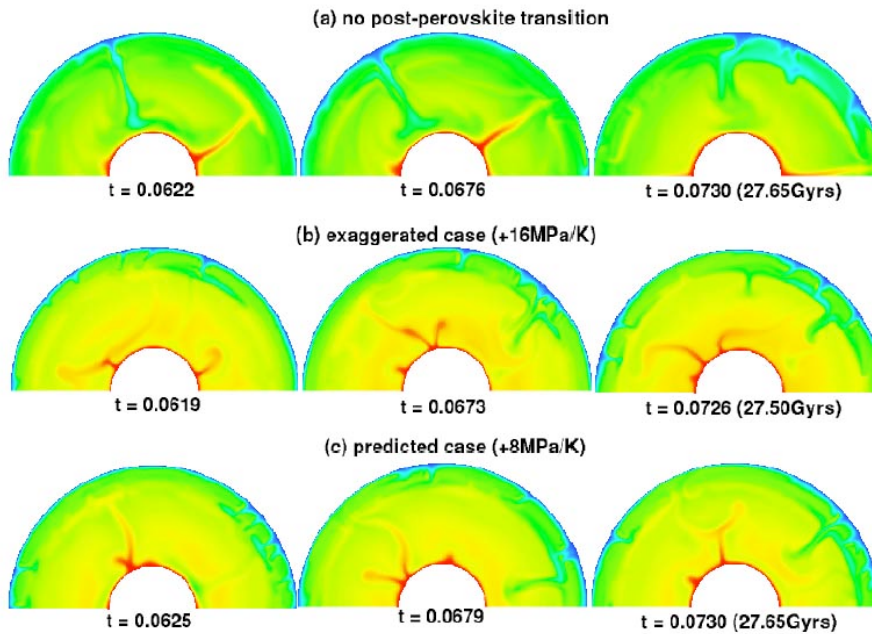
Figure 1 from Nakagawa and Tackley (2004). Time variation of the temperature field for (a) reference case with no post-perovskite transition (b) exaggerated case with doubled Clapeyron slope and (c) case with realistic Clapeyron slope. Quoted times are nondimensional, with a dimensional equivalent given for the final frame. Red indicates high temperature and blue indicates low temperature.

The exothermic ppp phase change destabilizes the lower thermal boundary layer and increases the heat flow, increases mantle temperature, and increases the number and time dependence of plumes. The resulting weak, highly time-dependent plumes have a smaller horizontal spacing than do plumes in the absence of the phase change.

P= −0.15   k=1

P= 0.15   k=1

T=0   T=1
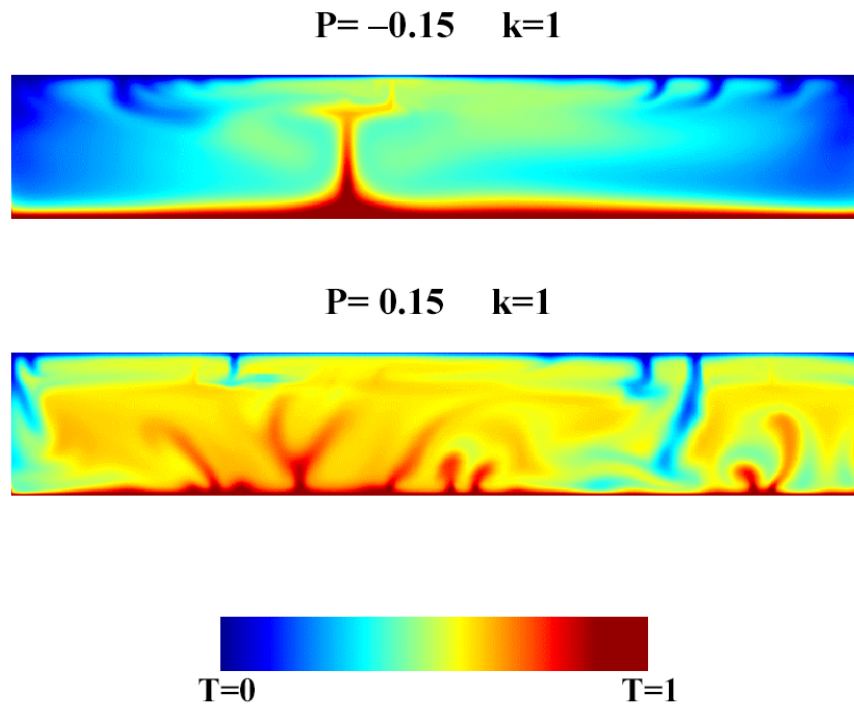
Figure 5 from Matyska and Yuen (2004). Snapshots of the temperature field for a deep mantle phase change with large absolute values of the buoyancy parameter. The endothermic deep mantle phase change with $P = −0.15$ produces a stable superplume but an exothermic phase change with $P = 0.15$ results in a chaotic behavior of the lower mantle.

While the sp $\rightarrow$ pv phase change on Mars promotes a superplume, the pv $\rightarrow$ ppp on Earth acts to make a superplume less likely.

Breuer et al. (1997, 1998) found that the ol $\rightarrow$ sp phase transition in the Martian mantle tends to inhibit upwelling plumes and concentrate upflow into a single large upflow. They attribute this to the latent heat effects (see Table above) which act opposite to phase boundary distortion. It is not obvious why the ol $\rightarrow$ sp transition would affect convection differently in Earth and Mars.

References

Bertka, C.M. and Y. Fei, 1997. Mineralogy of the Martian interior up to core-mantle boundary pressures. J. Geophys. Res., 102, 5251-5264.

Bertka, C.M. and Y. Fei, 1998. Implications of Mars Pathfinder data for the accretion history of the terrestrial planets. Science, 281, 1838-1840.

Breuer, D., D.A. Yuen, and T. Spohn, 1997. Phase transitions in the Martian mantle: Implications for partially layered convection. Earth Planet. Sci. Lett., 148, 457-469.

Breuer, D., D.A. Yuen, T. Spohn, and S. Zhang, 1998. Three-dimensional models of Martian mantle convection with phase transitions. Geophys. Res. Lett., 25, 229-232.

Cohen, E.R. and B. N.Taylor, 1999. The fundamental physical constants. Phys. Today, 52, BG5-BG-9.

Folkner, W.M., C.F. Yoder, D.N. Yuan, E.M. Standish, and R.A. Preston, 1997. Interior structure and seasonal mass redistribution of Mars from radio tracking of Mars Pathfinder. Science, 278, 1749-1751.

Gudkova, T.V. and V.N. Zharkov, 2004. Mars: Interior structure and excitation of free oscillations. Phys. Earth Planet. Inter., 142, 1-22.

Harder, H., 1998. Phase transitions and the three-dimensional planform of thermal convection in the Martian mantle. J. Geophys. Res., 103, 16,775-16, 797.

Harder, H. and U.R. Christensen, 1996. A one-plume model of Martian mantle convection. Nature, 380, 507-509.

Kaula, W.M., 1979. The moment of inertia of Mars. Geophys. Res. Lett., 6, 194-196.

Kavner, A., T.S. Duffy, and G. Shen, 2001. Phase stability and density of FeS at high pressures and temperatures: Implications for the interior structure of Mars. Earth Planet. Sci. Lett., 185, 25-33.

Lemoine, F.G., D.E. Smith, D.D. Rowlands, M.T. Zuber, G. A Neumann, D.S. Chinn, and D.E. Pavlis, 2001. An improved solution of the gravity field of Mars (GMM-2B) from Mars Global Surveyor. J. Geophys. Res., 106, 23,359-23,376.

Matyska, C. and D. Yuen, 2004. The importance of radiative heat transfer for superplumes with a deep mantle phase transition. Earth Planet. Sci. Lett., submitted, 2004.

Murakami, M., K. Hirose, K. Kawamura, N. Sata, and Y. Ohishi, 2004. Post-perovskite phase transition in $MgSiO_3$. Science, 304, 855-858.

Nakagawa, T. and P.J. Tackley, 2004. Effects of a perovskite-post perovskite phase change near core-mantle boundary in compressible mantle convection. Geophys. Res. Lett., in press.

Neumann, G.A., M.T. Zuber, M.A. Wieczorek, P.J. McGovern, F.G. Lemoine, and D.E. Smith, 2004. Crustal structure of Mars from gravity and topography. J. Geophys. Res., 109, E08002, doi:10.1029/2004/JE002262.

Oganov, A.R. and S. Ono, 2004. Theoretical and experimental evidence for a post-perovskite phase of $MgSiO_3$ in Earth's D´´ layer. Nature, 430, 445-448.

Schubert,G., D.L. Turcotte, and P. Olson, 2001. Mantle Convection in the Earth and Planets, Cambridge University Press, Cambridge, UK.

Smith, D.E., W.L. Sjogren, G. L. Tyler, G. Balmino, F.G. Lemoine, and A.S. Konopliv, 1999. The gravity field of Mars: Results from Mars Global Surveyor. Science, 286, 94-97.

Sohl, F. and T. Spohn, 1997. The interior structure of Mars: Implications from SNC meteorites. J. Geophys. Res., 102, 1613-1635.

Tsuchiya, T., J. Tsuchiya, K. Umemoto, and R.M. Wentzcovitch, 2004. Phase transition in $MgSiO_3$ perovskite in the Earth's lower mantle, Science, submitted, 2004.

Turcotte, D.L. and G. Schubert, 1982. Geodynamics, John Wiley, New York.

Turcotte, D.L., R. Shcherbakov, B.D. Malamud, and A.B. Kucinskas, 2002. Is the Martian crust also the Martian elastic lithosphere? J. Geophys. Res., 107, 5091, doi:10.1029/2001JE001594.

Van Hoolst, T. V. Dehant, F. Roosbeek, and P. Lognonné, 2003. Tidally induced surface displacements, external potential variations, and gravity variations on Mars. Icarus, 161, 281-296.

Wänke, H. and G. Dreibus, 1988. Chemical composition and accretion history of terrestrial planets. Phil. Trans. R. Soc. London, A325, 545-557.

Weinstein, S.A., 1995. The effects of a deep mantle endothermic phase change on the structure of thermal convection in silicate planets. J. Geophys. Res., 100, 11,719-11,728.

Wieczorek, M.A. and M.T. Zuber, 2004. Thickness of the Martian crust: Improved constraints from geoid-to-topgraphy ratios. J. Geophys. Res., 109, E01009, doi:10.1029/2003JE002153.

Yoder, C.F., A.S. Konopliv, D.N. Yuan, E.M. Standish, and W.M. Folkner, 2003. Fluid core size of Mars from detection of the solar tide. Science, 300, 299-303.

Zuber, M.T., S.C. Solomon, R.J. Phillips, D.E. Smith, G.L.Tyler, O. Aharonson, G. Balmino, W.B. Banerdt, J.W. Head, C.L. Johnson, F.G. Lemoine, P.J. McGovern, G.A. Neumann, D.D. Rowlands, and S. Zhong, 2000. Internal structure and early thermal evolution of Mars from Mars Global Surveyor topography and gravity. Science, 287, 1788-1793.